1-1-2008

Electroproduction of phi(1020) mesons at 1.4 <= Q(2) <= 3.8 GeV2 measured with the CLAS spectrometer

J. P. Santoro

Angela Biselli
Fairfield University, abiselli@fairfield.edu

CLAS Collaboration

Peer Reviewed

Published Citation

J. P. Santoro et al. [CLAS Collaboration], "Electroproduction of phi(1020) mesons at 1.4 <= Q(2) <= 3.8 GeV2 measured with the CLAS spectrometer", Physical Review C 78.2 (2008) DOI: 10.1103/PhysRevC.78.025210

Electroproduction of $\phi(1020)$ mesons at $1.4 \leqslant Q^2 \leqslant 3.8$ GeV^2 measured with the CLAS spectrometer

J. P. Santoro,[1,2] E. S. Smith,[3] M. Garçon,[4] M. Guidal,[5] J. M. Laget,[3] C. Weiss,[3] G. Adams,[35] M. J. Amaryan,[33] M. Anghinolfi,[22] G. Asryan,[43] G. Audit,[4] H. Avakian,[3] H. Bagdasaryan,[33,43] N. Baillie,[42] J. Ball,[4] J. P. Ball,[7] N. A. Baltzell,[39] S. Barrow,[17] M. Battaglieri,[22] I. Bedlinskiy,[24] M. Bektasoglu,[33,*] M. Bellis,[10] N. Benmouna,[18] B. L. Berman,[18] A. S. Biselli,[15,35] L. Blaszczyk,[17] B. E. Bonner,[36] C. Bookwalter,[17] S. Bouchigny,[5] S. Boiarinov,[3,24] R. Bradford,[10] D. Branford,[13] W. J. Briscoe,[18] W. K. Brooks,[38] S. Bültmann,[33] V. D. Burkert,[3] C. Butuceanu,[42] J. R. Calarco,[30] S. L. Careccia,[33] D. S. Carman,[3] L. Casey,[2] A. Cazes,[39] S. Chen,[17] L. Cheng,[2] P. L. Cole,[3,20] P. Collins,[7] P. Coltharp,[17] D. Cords,[3,†] P. Corvisiero,[22] D. Crabb,[41] H. Crannell,[2] V. Crede,[17] J. P. Cummings,[35] D. Dale,[20] N. Dashyan,[43] R. De Masi,[4] E. De Sanctis,[21] R. De Vita,[22] P. V. Degtyarenko,[3] H. Denizli,[34] L. Dennis,[17] A. Deur,[3] S. Dhamija,[16] K. V. Dharmawardane,[33] K. S. Dhuga,[18] R. Dickson,[10] C. Djalali,[39] G. E. Dodge,[33] D. Doughty,[3,11] M. Dugger,[7] S. Dytman,[34] O. P. Dzyubak,[39] H. Egiyan,[3,42,‡] K. S. Egiyan,[43,†] L. El Fassi,[6] L. Elouadrhiri,[3] P. Eugenio,[17] R. Fatemi,[41] G. Fedotov,[29] R. J. Feuerbach,[10] J. Ficenec,[1] T. A. Forest,[20] A. Fradi,[5] H. Funsten,[42,†] G. Gavalian,[30,33] N. Gevorgyan,[43] G. P. Gilfoyle,[37] K. L. Giovanetti,[25] F. X. Girod,[4] J. T. Goetz,[8] W. Gohn,[12] C. I. O. Gordon,[19] R. W. Gothe,[39] L. Graham,[39] K. A. Griffioen,[42] M. Guillo,[39] N. Guler,[33] L. Guo,[3] V. Gyurjyan,[3] C. Hadjidakis,[5] K. Hafidi,[6] H. Hakobyan,[43] C. Hanretty,[17] J. Hardie,[3,11] N. Hassall,[19] D. Heddle,[3,§] F. W. Hersman,[30] K. Hicks,[32] I. Hleiqawi,[32] M. Holtrop,[30] C. E. Hyde-Wright,[33] Y. Ilieva,[18] D. G. Ireland,[19] B. S. Ishkhanov,[29] E. L. Isupov,[29] M. M. Ito,[3] D. Jenkins,[1] H. S. Jo,[5] J. R. Johnstone,[19] K. Joo,[3,12] H. G. Juengst,[33] N. Kalantarians,[33] D. Keller,[32] J. D. Kellie,[19] M. Khandaker,[31] W. Kim,[26] A. Klein,[33] F. J. Klein,[2] A. V. Klimenko,[33] M. Kossov,[24] Z. Krahn,[10] L. H. Kramer,[3,16] V. Kubarovsky,[3] J. Kuhn,[10,35] S. E. Kuhn,[33] S.V. Kuleshov,[24] V. Kuznetsov,[26] J. Lachniet,[10,33] J. Langheinrich,[39] D. Lawrence,[28] Ji Li,[35] K. Livingston,[19] H. Y. Lu,[39] M. MacCormick,[5] C. Marchand,[4] N. Markov,[12] P. Mattione,[36] S. McAleer,[17] B. McKinnon,[19] J. W. C. McNabb,[10] B. A. Mecking,[3] S. Mehrabyan,[34] J. J. Melone,[19] M. D. Mestayer,[3] C. A. Meyer,[10] T. Mibe,[32] K. Mikhailov,[24] R. Minehart,[41] M. Mirazita,[21] R. Miskimen,[28] V. Mokeev,[3,29] L. Morand,[4] B. Moreno,[5] K. Moriya,[10] S. A. Morrow,[4,5] M. Moteabbed,[16] J. Mueller,[34] E. Munevar,[18] G. S. Mutchler,[36] P. Nadel-Turonski,[18] R. Nasseripour,[16,39,‖] S. Niccolai,[5,18] G. Niculescu,[25,32] I. Niculescu,[3,18,25] B. B. Niczyporuk,[3] M. R. Niroula,[33] R. A. Niyazov,[33,35] M. Nozar,[3] G. V. O'Rielly,[18] M. Osipenko,[22] A. I. Ostrovidov,[17] K. Park,[26,39] S. Park,[17] E. Pasyuk,[7] C. Paterson,[19] S. Anefalos Pereira,[21] S. A. Philips,[18] J. Pierce,[41] N. Pivnyuk,[24] D. Pocanic,[41] O. Pogorelko,[24] I. Popa,[18] S. Pozdniakov,[24] B. M. Preedom,[39] J. W. Price,[9] S. Procureur,[4] Y. Prok,[41,¶] D. Protopopescu,[19,30] L. M. Qin,[33] B. A. Raue,[3,16] G. Riccardi,[17] G. Ricco,[22] M. Ripani,[22] B. G. Ritchie,[7] G. Rosner,[19] P. Rossi,[21] F. Sabatié,[4] M. S. Saini,[17] J. Salamanca,[20] C. Salgado,[31] V. Sapunenko,[3] D. Schott,[16] R. A. Schumacher,[10] V. S. Serov,[24] Y. G. Sharabian,[3] D. Sharov,[29] N. V. Shvedunov,[29] A. V. Skabelin,[27] L. C. Smith,[41] D. I. Sober,[2] D. Sokhan,[13] A. Stavinsky,[24] S. S. Stepanyan,[26] S. Stepanyan,[3] B. E. Stokes,[17] P. Stoler,[35] I. I. Strakovsky,[18] S. Strauch,[18,39] M. Taiuti,[22] D. J. Tedeschi,[39] A. Tkabladze,[18,*] S. Tkachenko,[33] L. Todor,[10,**] C. Tur,[39] M. Ungaro,[12,35] M. F. Vineyard,[37,40] A. V. Vlassov,[24] D. P. Watts,[19,††] L. B. Weinstein,[33] D. P. Weygand,[3] M. Williams,[10] E. Wolin,[3] M. H. Wood,[39,‡‡] A. Yegneswaran,[3] M. Yurov,[26] L. Zana,[30] J. Zhang,[33] B. Zhao,[12] and Z. W. Zhao[39]

(CLAS Collaboration)

[1]*Virginia Polytechnic Institute and State University, Blacksburg, Virginia 24061-0435, USA*
[2]*Catholic University of America, Washington, DC 20064, USA*
[3]*Thomas Jefferson National Accelerator Facility, Newport News, Virginia 23606, USA*
[4]*CEA-Saclay, Service de Physique Nucléaire, F-91191 Gif-sur-Yvette, France*
[5]*Institut de Physique Nucleaire ORSAY, Orsay, France*
[6]*Argonne National Laboratory, Argonne, Illinois 60439, USA*
[7]*Arizona State University, Tempe, Arizona 85287-1504, USA*
[8]*University of California at Los Angeles, Los Angeles, California 90095-1547, USA*
[9]*California State University, Dominguez Hills, Carson, California 90747, USA*
[10]*Carnegie Mellon University, Pittsburgh, Pennsylvania 15213, USA*
[11]*Christopher Newport University, Newport News, Virginia 23606, USA*
[12]*University of Connecticut, Storrs, Connecticut 06269, USA*
[13]*Edinburgh University, Edinburgh EH9 3JZ, United Kingdom*
[14]*Emmy-Noether Foundation, Germany*
[15]*Fairfield University, Fairfield, Connecticut 06824, USA*
[16]*Florida International University, Miami, Florida 33199, USA*
[17]*Florida State University, Tallahassee, Florida 32306, USA*
[18]*George Washington University, Washington, DC 20052, USA*
[19]*University of Glasgow, Glasgow G12 8QQ, United Kingdom*
[20]*Idaho State University, Pocatello, Idaho 83209, USA*
[21]*INFN, Laboratori Nazionali di Frascati, I-00044 Frascati, Italy*
[22]*INFN, Sezione di Genova, I-16146 Genova, Italy*
[23]*Institute für Strahlen und Kernphysik, Universität Bonn, Germany*
[24]*Institute of Theoretical and Experimental Physics, RU-117259 Moscow, Russia*

[25]*James Madison University, Harrisonburg, Virginia 22807, USA*
[26]*Kyungpook National University, Daegu 702-701, Republic of Korea*
[27]*Massachusetts Institute of Technology, Cambridge, Massachusetts 02139-4307, USA*
[28]*University of Massachusetts, Amherst, Massachusetts 01003, USA*
[29]*Moscow State University, General Nuclear Physics Institute, RU-119899 Moscow, Russia*
[30]*University of New Hampshire, Durham, New Hampshire 03824-3568, USA*
[31]*Norfolk State University, Norfolk, Virginia 23504, USA*
[32]*Ohio University, Athens, Ohio 45701, USA*
[33]*Old Dominion University, Norfolk, Virginia 23529, USA*
[34]*University of Pittsburgh, Pittsburgh, Pennsylvania 15260, USA*
[35]*Rensselaer Polytechnic Institute, Troy, New York 12180-3590, USA*
[36]*Rice University, Houston, Texas 77005-1892, USA*
[37]*University of Richmond, Richmond, Virginia 23173, USA*
[38]*Universidad Técnica Federico Santa María, Casilla 110-V, Valparaíso, Chile*
[39]*University of South Carolina, Columbia, South Carolina 29208, USA*
[40]*Union College, Schenectady, New York 12308, USA*
[41]*University of Virginia, Charlottesville, Virginia 22901, USA*
[42]*College of William and Mary, Williamsburg, Virginia 23187-8795, USA*
[43]*Yerevan Physics Institute, 375036 Yerevan, Armenia*
(Received 28 March 2008; published 18 August 2008)

Electroproduction of exclusive ϕ vector mesons has been studied with the CLAS detector in the kinematic range $1.4 \leqslant Q^2 \leqslant 3.8\,\mathrm{GeV}^2$, $0.0 \leqslant t' \leqslant 3.6\,\mathrm{GeV}^2$, and $2.0 \leqslant W \leqslant 3.0\,\mathrm{GeV}$. The scaling exponent for the total cross section as $1/(Q^2 + M_\phi^2)^n$ was determined to be $n = 2.49 \pm 0.33$. The slope of the four-momentum transfer t' distribution is $b_\phi = 0.98 \pm 0.17\,\mathrm{GeV}^{-2}$. Under the assumption of s-channel helicity conservation, we determine the ratio of longitudinal to transverse cross sections to be $R = 0.86 \pm 0.24$. A two-gluon exchange model is able to reproduce the main features of the data.

DOI: 10.1103/PhysRevC.78.025210 PACS number(s): 13.60.Le, 12.40.Nn, 12.40.Vv, 25.30.Rw

I. INTRODUCTION

Exclusive electroproduction of vector mesons is an essential tool for exploring the structure of the nucleon and the exchange mechanisms governing high-energy scattering. For low photon virtualities relative to the vector meson mass, $Q^2 \lesssim m_V^2$, or in the case of photoproduction, $Q^2 = 0$, these processes are well described by t-channel exchange of Regge poles (Pomeron, Reggeon)—extended objects whose properties can be related to the observed hadron spectrum [1]. At high virtualities, $Q^2 \gg m_V^2$, a QCD factorization theorem [2] states that vector meson production from longitudinally polarized photons proceeds by exchange of a small-size system of quarks or gluons, whose coupling to the nucleon is described by the generalized parton distributions (GPDs). By studying the dependence of exclusive electroproduction on Q^2, one can thus "resolve" the Pomeron and Reggeon into their quark and gluon constituents. Additional information comes from the comparison of the ρ^0, ω, and ϕ channels, which couple differently to quarks and gluons. The self-analyzing decays of the spin-1 mesons allow one to study also the helicity structure of the $\gamma^* N$ interaction and, assuming helicity conservation, to separate longitudinal and transverse photon polarizations.

This article presents data for exclusive ϕ vector meson electroproduction off the proton above the resonance region, taken with a 5.754 GeV electron beam of the continuous electron beam accelerator facility (CEBAF) accelerator and the CEBAF large acceptance spectrometer (CLAS) detector at the Thomas Jefferson National Accelerator Facility (JLab) [3]. The measurement was performed as part of a series of experiments aimed at studying vector meson production in the valence quark region at the highest available photon virtualities. The analysis of ω production has been completed [4], and the analysis of ρ production is in progress [5]. The analysis of ϕ-meson production reported here is based in part on the work of Ref. [6].

The ϕ meson is unique in that its quark composition is mostly $\bar{s}s$ containing little, if any, u and d flavors which populate the valence quarks in the nucleon. Thus, ϕ

*Current address: Ohio University, Athens, Ohio 45701, USA.
†Deceased.
‡Current address: University of New Hampshire, Durham, New Hampshire 03824-3568, USA.
§Current address: Christopher Newport University, Newport News, Virginia 23606, USA.
‖Current address: George Washington University, Washington, DC 20052, USA.
¶Current address: Massachusetts Institute of Technology, Cambridge, Massachusetts 02139-4307, USA.
**Current address: University of Richmond, Richmond, Virginia 23173, USA.
††Current address: Edinburgh University, Edinburgh EH9 3JZ, United Kingdom.
‡‡Current address: University of Massachusetts, Amherst, Massachusetts 01003, USA.

production primarily probes the gluon degrees of freedom in the target. High-energy photoproduction of ϕ proceeds mainly by Pomeron exchange. At large Q^2, calculations based on current GPD models show that the ϕ production cross section is dominated by the gluon GPD, with only small contributions arising from intrinsic strange quarks in the nucleon [7,8]. At intermediate Q^2, a description of ϕ production based on effective two-gluon exchange has been proposed [9], which effectively interpolates between the "soft" and "hard" regimes. Thus, ϕ production provides us with a clean method of probing the gluon field in the nucleon, even at JLab energies.

A natural framework for discussing exclusive vector meson production is the space-time picture in the target rest frame (i.e., the laboratory frame) [10]. At high energies, the interaction of the virtual photon with the target proton proceeds by way of fluctuation of the photon into virtual hadronic (or quark-antiquark) configurations that subsequently scatter diffractively off the target. This process occurs over a characteristic time given by the lifetime of the fluctuation as dictated by the uncertainty principle and is given by

$$\Delta\tau = \frac{2\nu}{Q^2 + M_{\rm fluct}^2}, \tag{1}$$

where ν is the photon laboratory energy and $M_{\rm fluct}$ is the mass of the virtual hadronic state. This interval also determines the coherence length in the longitudinal direction, $l_{\rm coh} = c\Delta\tau$. In photoproduction or electroproduction at $Q^2 \lesssim m_V^2$, this picture is the basis for the successful vector dominance model (VDM), where the dominant hadronic fluctuations are assumed to be the observed ground-state vector mesons (ρ^0, ω, ϕ). Their interaction with the target can be described by Pomeron exchange. As Q^2 increases, higher mass states become important. Eventually, at $Q^2 \gg m_V^2$, the fluctuations of the photon can appropriately be described as quark-antiquark pairs ("dipoles") with transverse momenta $k_\perp^2 \sim Q^2$, or transverse size $r_\perp \sim 1/Q \ll 1/m_V$. Their interaction with the nucleon is described by the gluon GPD, which can be interpreted as the "color dipole moment" of the target.

In the context of the space-time picture, measuring the Q^2 dependence of exclusive electroproduction up to $Q^2 \sim$ few GeV^2 allows one to vary the transverse size of the projectile from "hadronic size" ($r_\perp \sim 1/m_V$) to "small size" ($r_\perp \sim 1/Q$), thus resolving the structure of the target at very different distance scales. At HERA energies, where $l_{\rm coh} \gg 1$ fm even for $Q^2 \sim$ few GeV^2, one can neglect the variation of the coherence length with Q^2 and associate the Q^2 dependence entirely with a change of the transverse size of the projectile. The predictions derived in this approximation are nicely confirmed by the data, e.g., the decrease of the t slope with Q^2, and the increase with Q^2 of the exponent governing the energy dependence (for a review, see Ref. [11]). At JLab energies, where the coherence length in electroproduction is $l_{\rm coh} \lesssim 1$ fm, we must also take into account its variation with Q^2, i.e., the "shrinkage" of the longitudinal size of the virtual photon with increasing Q^2. Another effect modifying the space-time interpretation is the nonnegligible longitudinal momentum transfer to the target, which increases with Q^2. Nevertheless, the space-time picture remains a very useful framework for discussing vector meson electroproduction even at JLab energies.

In the present ϕ-meson production experiment, the t dependence of the differential cross section was measured over a wide range, from the kinematic minimum at $t \sim t_0$ (small c.m. scattering angle) to $t \sim s/2$ (large angle). In exclusive electroproduction, t is related to the transverse momentum transfer to the target, $\Delta_\perp^2$, and thus determines the effective impact parameters in the cross section, $b_\perp \sim 1/\Delta_\perp$.[1] Exclusive meson production at large $-(t - t_0)$ probes configurations of small transverse size in the target. The possibility of varying both Q^2 and t in electroproduction allows one to control both the size of the projectile and the size of the target configurations contributing to the process, and to study their interplay [12].

Quantitative predictions of the production of vector mesons in our kinematic regime have been made by Laget and collaborators based on the interactions between constituent partons (JML model). The high-t behavior of the photoproduction cross section of ϕ mesons [13] has been reproduced using dressed gluon propagators and correlated quark wave functions in the proton [14]. Quark exchange processes, which contribute also to the photoproduction of ρ and ω mesons, have been modeled in terms of saturating Regge trajectories. The model uses electromagnetic form factors in the Regge amplitude [12,15] to describe electroproduction data. However, the Q^2 dependence of the two-gluon amplitude is an intrinsic part of its construction, and no additional electromagnetic form factors are needed. Therefore, the predicted ϕ-meson electroproduction cross section is parameter free and constitutes a strong test of the partonic description that underlies the model. The full form for the amplitudes are given in Refs. [1,9,14]. Thus far, comparisons of the JML model for electroproduction have been made with ω [4,16] and ρ [5,17] electroproduction data from JLab, and ρ electroproduction data from the HERMES [18] experiment at DESY.

One of the leading motivations for the present work is the sparse amount of existing ϕ electroproduction data. The body of ϕ-meson electroproduction data at similar kinematics consists of early data from Cornell [19–21] and some data from CLAS at lower energy [22]. Recent data on ϕ electroproduction comes from HERMES [18,23] and HERA [24–27] at much higher center-of-mass energy W. A summary of the world data indicating their kinematic range is given in Table I. The data from this experiment are complementary to measurements at collider energies that cover a higher W and higher Q^2 range where diffraction mechanisms are probed.

We have measured ϕ-meson electroproduction at the highest possible Q^2 accessible at CEBAF energies in the valence quark regime. The data set covers the kinematic regime $1.4 \leqslant Q^2 \leqslant 3.8$ GeV^2, $0.0 \leqslant t' \leqslant 3.6$ GeV^2, and $2.0 \leqslant W \leqslant 3.0$ GeV. We will present cross sections as a function of the momentum transfer $-t$, the azimuthal angle Φ between the

[1]The transverse momentum transfer to the target is given by $\Delta_\perp^2 = (1 - \xi^2)(t - t_0)$, where ξ is the fractional longitudinal momentum transfer to the target, which in turn is related to the Bjorken variable in the kinematics of deep-inelastic scattering, $\xi = x_B/(2 - x_B)$.

TABLE I. Summary of ϕ electroproduction data and kinematic range.

Experiment	Q^2 (GeV^2)	W (GeV)
Cornell Dixon [19,20]	0.23–0.97	2.9
Cornell Cassel [21]	0.80–4.00	2.0–3.7
HERMES [18,23]	0.70–5.00	4.0–6.0
CLAS [22]	0.70–2.20	2.0–2.6
H1 [24]	>7.0	∼75.0
H1 [25]	1.00–15.0	40.0–130.0
H1 [27]	3.00–20.0	4.0–120.0
ZEUS [26]	7.00–25.0	42.0–134.0
ZEUS [26]	2.00–70.0	35–145

electron and hadron scattering planes, as well as the angular decay distributions in the rest frame of the ϕ meson. Although limitations of the statistical sample will preclude determining correlations between different kinematic variables, the distributions will provide insight into the distance scale of the interaction and allow one to explore kinematics that begin to probe partonic degrees of freedom.

II. KINEMATICS AND NOTATION

The kinematic variables in exclusive ϕ production (see Fig. 1) described by

$$e(k)\, p(P) \rightarrow e(k')\phi(\upsilon) p(P'), \tag{2}$$

are k, k', P, P', and υ, which are, respectively, the four-momenta of the incident electron, scattered electron, target proton, scattered proton, and the ϕ meson:

(i) $Q^2 = -q^2 = -(k - k')^2$, the negative four-momentum squared of the virtual photon;

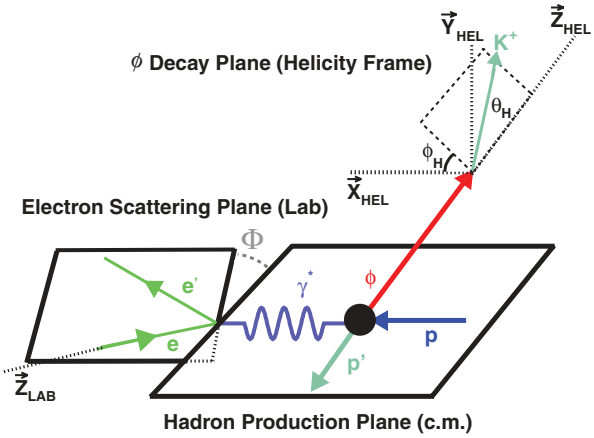

FIG. 1. (Color online) Graphical representation of ϕ-meson electroproduction. Shown from left to right then above are the electron scattering plane, the hadron production plane, and helicity rest frame of the ϕ, respectively.

(ii) $W^2 = (q + P)^2$, the squared invariant mass of the photon-proton system;

(iii) $x_B = Q^2/(2P \cdot q)$, the Bjorken scaling variable;

(iv) $\nu = P \cdot q/M_p$, energy of the virtual photon;

(v) $t = (P - P')^2$, the squared four-momentum transfer at the proton vertex, is given by

$$t = t_0 - 4p^{\gamma^*}_{\text{c.m.}} p^{\phi}_{\text{c.m.}} \sin^2(\theta_{\text{c.m.}}/2), \quad \text{where}$$
$$t_0 = \left(E^{\gamma^*}_{\text{c.m.}} - E^{\phi}_{\text{c.m.}}\right)^2 - \left(p^{\gamma^*}_{\text{c.m.}} - p^{\phi}_{\text{c.m.}}\right)^2$$

and the above formulas are calculated using the energy and momenta of the virtual photon and ϕ in the $\gamma^* p$ center-of-mass;

(vi) $t' = |t - t_0|$, momentum transfer relative to the kinematic limit $-t_0$, which increases with Q^2 and decreases with increasing W;

(vii) Coordinate system in the $\gamma^* p$ center-of-mass defined with the z axis along the direction of the virtual photon, and the y axis normal to the hadronic production plane along $\vec{p}^{\,\gamma^*}_{\text{c.m.}} \times \vec{p}^{\,\phi}_{\text{c.m.}}$;

(viii) Φ, the angle between the hadron production ($\gamma^*\phi p$) plane and the electron scattering ($ee'\gamma^*$) plane following the convention in Ref. [28][2];

(ix) $\cos\theta_H$ and ϕ_H, the decay angles of the K^+ in the helicity frame [28], which is defined in the rest frame of the ϕ meson with the z axis along the direction of the ϕ meson in the $\gamma^* p$ center-of-mass system;

(x) $\psi = \phi_H - \Phi$, the azimuthal angle that simplifies the angular decay distributions when s-channel helicity is conserved (SCHC).

The electroproduction reaction integrated over the decay angles of the ϕ meson can be described by the following set of four independent variables: Q^2, $-t$, Φ, and W. For the analysis of the decay distribution, the additional variables $\cos\theta_H$ and ψ are required. In total, there are six independent variables in the approximation of negligible ϕ width.

III. EXPERIMENT

The experiment was conducted with the CEBAF large acceptance spectrometer (CLAS) [3] located in Hall B of JLab. CLAS is built around six independent superconducting coils that generate a toroidal magnetic field azimuthally around the beam direction. The azimuthal coverage is limited by the magnetic coils and is approximately 90% at large angles and narrows to 50% at forward angles. Each sector is equipped with three regions of multi-wire drift chambers and time-of-flight counters that cover the angular range from 8° to 143°. Charged-particle trajectories are tracked through the field with the drift chambers, and the scintillators provide a precise determination of the particle flight time. In the forward region (8° to 45°), each sector is furthermore equipped with gas-filled threshold Cherenkov counters (CC) and electromagnetic calorimeters

[2]The azimuthal angle Φ used here is $-\phi$ from the "Trento convention" [29].

(EC). The Cherenkov counters are used to discriminate electrons from pions, and the calorimeters are used to measure the energy of electrons and photons.

The data were collected between October 2001 and January 2002 with a 5.754 GeV electron beam incident on a 5-cm-long liquid hydrogen target. The typical beam current was 7 nA. The CLAS torus magnet was set to 3375 A with a polarity that caused negatively charged particles to bend in toward the beamline. The inclusive electron trigger fired when signals in the forward electromagnetic calorimeter exceeded a predefined threshold in coincidence with a hit in the CCs. The kinematic domain of the selected sample corresponded approximately to Q^2 from 1.5 to 5.5 GeV^2 and W between 2 and 3 GeV. The typical experimental dead time was about 8% with a trigger rate of about 1.5 kHz.

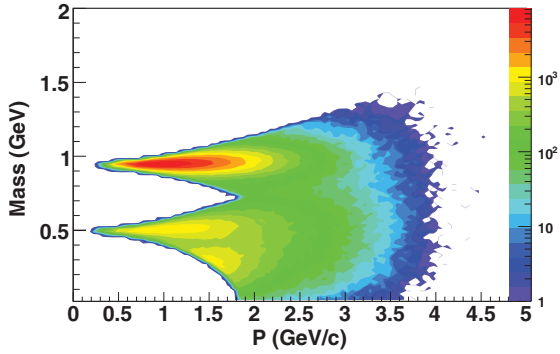

FIG. 3. (Color) Mass computed from the flight time vs momentum for positive particles. The top band corresponds to protons, the middle band corresponds to K^+'s, and the lower enhancement at 1.5 GeV/c momentum is due to pion contamination.

IV. EVENT RECONSTRUCTION

The ϕ mesons were detected using the charged-particle decay mode into K^+ and a K^-. Events corresponding to $ep \to epK^+(K^-)$ were classified initially by requiring at least one negative track and two positive tracks. Normally the K^- remained undetected because of the limited acceptance for negative particles at this high magnetic field setting. After calibration of the spectrometer, the momentum of each particle was determined with a fractional resolution of about 1% using the track segments in the drift chambers. The momentum resolution is sufficient to identify the missing particle as a K^-.

The identification of good electrons is the crucial first step and is accomplished through energy and momentum cuts [6]. After selection of tracks within the fiducial volume of the detector, the momentum of the electron candidate track in each event was required to correspond to the energy deposition in the electromagnetic calorimeter and the visible energy be greater than 0.2 GeV (Fig. 2). Pions were rejected by requiring a minimum energy of 0.06 GeV in the inner layer of the calorimeter and a pulse height in the CC corresponding to at least 2.5 photoelectrons [30,31].

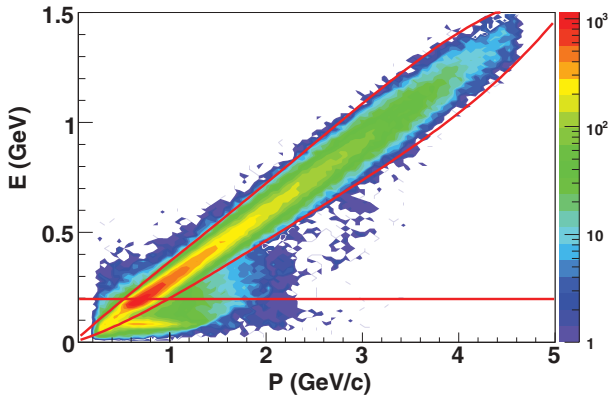

FIG. 2. (Color) Energy deposited by the electron candidates in the electromagnetic calorimeter vs momentum. The lines show the selection cuts for good electrons as described in the text.

The two positive tracks in the fiducial volume were identified as a proton and K^+ using the measured flight time ($\delta T \sim 160$ ps) from the target to the time-of-flight counters [32], a typical distance of about 5 m. Fiducial volume cuts were made to cut out tracks in inefficient parts of the detector, and small momentum corrections were applied to compensate for uncertainties in the magnetic field and detector positioning. The time of the interaction was determined using the vertex time of the electron corrected to the time of the bunch crossing of the machine. Using the known momenta of each of the tracks, the vertex time was computed making assumptions for the mass of the particle and comparing to the time of the bunch crossing. Events were kept for which the two positive tracks were consistent with the assignment of one proton and one K^+. Tracks were identified as protons when the projected vertex time assuming a proton mass differed from the interaction time by less than 0.75 ns, and as a K^+ when the projected time assuming a kaon mass differed from the interaction time by less than 0.6 ns. When one track satisfied both criteria, the ambiguity was resolved using the second track. The number of events for which both tracks satisfied both criteria was less than 1% and were eliminated. The calculated mass vs momentum, shown in Fig. 3, indicates that at high momenta, there remain a number of pions that are identified as kaons in the sample.

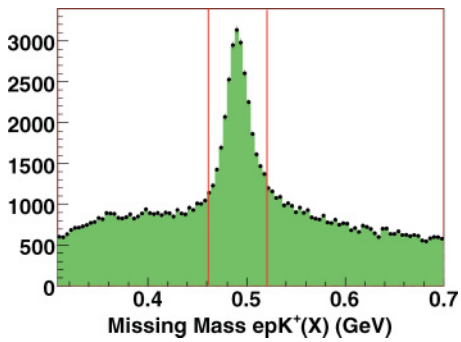

FIG. 4. (Color online) Distribution of epK^+X missing mass. The vertical lines indicate the cuts placed to select events with a missing K^-.

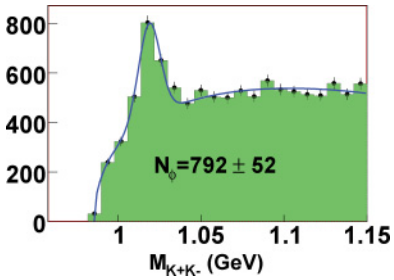

FIG. 5. (Color online) K^+K^- invariant mass including all data cuts and a fit to ϕ peak with Eq. (3).

Once the electron, proton, and K^+ tracks were identified, the missing mass was computed and is plotted in Fig. 4. A clear peak is found at the mass of the K^-, which corresponds to the exclusive reaction $ep \to epK^+K^-$. A 2σ cut was applied to the epK^+X events to select the sample of interest. For those events, the four-vector for the K^- was constructed by setting the three-momentum equal to the missing momentum of the $ep \to epK^+X$ reaction, and the energy was then calculated using the K^- mass recommended by the Particle Data Group [33]. The fraction of events where the K^- was detected in the detector was so small that they were not treated differently than the rest of the sample.

A. ϕ Event identification

The sample satisfying the $epK^+(K^-)$ criteria contains 27 950 events out of 947 300 epK^+X candidates. The sample includes all physical processes that contribute to this final state, as well as real ϕ's and background from misidentified pions. Figure 5 shows the K^+K^- invariant mass (M_{KK}) for the entire data set with a clear ϕ-meson peak. This distribution is simultaneously fit to a Gaussian plus an empirical phase-space function for the background,

$$\mathrm{FIT} = A\mathsf{G}(\sigma,\mu) + B_1\sqrt{{M_{kk}}^2 - M_{\mathrm{th}}^2} + B_2\left({M_{kk}}^2 - M_{\mathrm{th}}^2\right), \quad (3)$$

where $\mathsf{G}(\sigma,\mu)$ is a Gaussian distribution, $M_{\mathrm{th}} = 0.986$ GeV is the threshold for two kaon production and A, B_1, and B_2 are parameters of the fit. This fit yields $N_\phi = 792 \pm 52$, a mean $\mu = 1.0194 \pm 0.0005$ GeV, and a width of $\sigma = 6.5 \pm 0.6$ MeV. The signal-to-background ratio for this fit is 0.56. The mean and width are fixed to these values for all subsequent fits to the invariant mass distribution to constrain the fits with limited statistics in specific kinematic bins. A total of 37 distributions were fitted to extract the ϕ signal in various kinematic bins (see subsequent sections for details). The average χ^2 per degree of freedom for all the fits was 1.07, indicating that deviations from the fit function are statistical in nature.

There are competing physics channels that also lead to the same final state. The majority of these backgrounds come from the production and subsequent decay of high-mass hyperons produced via $ep \to e'K^+\Lambda^*(\Sigma^*)$ as illustrated in Fig. 6. The Dalitz plot in Fig. 7 clearly shows the dominant $\Lambda(1520)$ background contribution (horizontal strip), as well as the $\phi(1020)$ (vertical strip). There are additional contributions from the higher mass states such

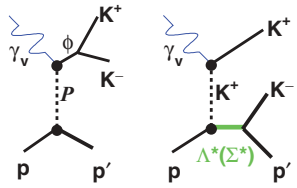

FIG. 6. (Color online) Sketch of exclusive $\phi(1020)$ production via Pomeron exchange and of excited hyperon production, of which $\Lambda(1520)$ is an example. This is the primary physics background for $\phi(1020)$ production.

as $\Lambda^*(1600)$, $\Lambda^*(1800)$, $\Lambda^*(1820)$, $\Sigma^*(1660)$, and $\Sigma^*(1750)$, but they cannot be separately identified. To avoid the introduction of holes in the acceptance, no cuts are made to remove these hyperon backgrounds. Instead, they are taken into account during the fitting procedure by assuming they contribute to the smooth background under the ϕ-meson peak. Nevertheless, many different fits were performed removing events in the peak of the $\Lambda^*(1520)$ to study this systematic with no indication that they changed the results significantly. These studies focused on the t distributions, since the effective momentum transfer in Λ^* reactions is very flat compared to that expected from ϕ-meson production.

V. ACCEPTANCE CORRECTIONS

Particle interactions and event reconstruction in the detector were simulated using a GEANT-based Monte Carlo called GSIM [34]. The events were generated according to a VDM-inspired cross section [10] with the following form:

$$\sigma_\phi^{VDM}(Q^2, W) = \frac{\sigma_\phi(0, W)[1 + R\epsilon]}{\left(1 + Q^2/M_\phi^2\right)^3} \times \frac{\left(W^2 - M_p^2\right)\exp(-bt')}{\sqrt{\left(W^2 - {M_p}^2 - Q^2\right)^2 + 4W^2Q^2}} \quad (4)$$

$$\epsilon = \frac{4E_e(E_e - \nu) - Q^2}{4E_e(E_e - \nu) + 2\nu^2 + Q^2}, \quad (5)$$

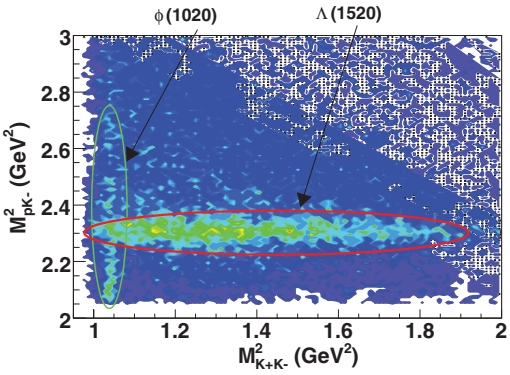

FIG. 7. (Color) Dalitz plot of M_{pK}^2 vs M_{KK}^2. The well-defined horizontal strip is the $\Lambda(1520)$ band. The vertical strip is the $\phi(1020)$ band.

TABLE II. Binning for the acceptance calculation in Q^2 (GeV^2), $-t$ (GeV^2), and W(GeV). An additional acceptance table was also generated for t' in the place of t, but it is not an independent variable.

	No.	Bin definition						
Q^2	5	1.4–1.8	1.8–2.2	2.2–2.6	2.6–3.0	3.0–3.8		
W	4	1.9–2.1	2.1–2.5	2.5–2.7	2.7–2.9			
$-t$	6	0.4–0.8	0.8–1.2	1.2–1.6	1.6–2.0	2.0–2.4	2.4–3.6	
t'	7	0.0–0.2	0.2–0.4	0.4–0.6	0.6–0.8	0.8–1.0	1.0–2.0	2.0–3.6

where $\sigma_\phi(0, W)$ is the (transverse) photoproduction cross section, E_e is the incident electron beam energy, ϵ is the virtual photon polarization parameter, and R is the ratio of the longitudinal to transverse cross section. The parameters of the model were tuned during preliminary analysis and found to reproduce the general features of the data. The main variation from the conventional VDM model was in the propagator, where preliminary data seemed to indicate a stronger dependence on Q^2 and an exponent of 3 was used instead of 2.

The acceptance function is a combination of the geometrical acceptance of CLAS, the detector efficiencies of the scintillators and drift chambers, the track reconstruction efficiency, and the event selection efficiency. The Cherenkov detector [30] is not well modeled in GSIM, and its efficiency was determined separately using the data.

The acceptance was defined in each bin of a six-dimensional table as the ratio of reconstructed to generated Monte Carlo events. To account for correlations between all kinematic variables, a total of 33 600 acceptance bins were defined in the kinematic variables Q^2, $-t$, W, Φ, $\cos\theta_H$, and ψ. The binning selection is given in Table II for the first three variables, and uniform binning was used for Φ (six bins), $\cos\theta_H$ (five bins), and ψ (eight bins). The projected two-dimensional (2-D) acceptance surface in Q^2 and $-t$ and the one-dimensional (1-D) projections in Q^2, t, and W are shown in Fig. 8. The projected 2-D acceptance surface in $\cos\theta_H$ and ψ is shown in Fig. 9, as well as the 1-D projections in $\cos\theta_H$, ψ, and Φ. The variation of the acceptance is relatively smooth as a function of these variables (except for Φ, which is a reflection of the CLAS torus coils) and is of the order of 1–3%.

Events that fell into bins with extremely small acceptances ($\leqslant$0.2%) were eliminated to avoid biases due to statistical fluctuations in those bins. The losses were estimated and corrected by using the ratio of Monte Carlo acceptance-weighted events to generated events.

VI. RADIATIVE CORRECTIONS

The radiative effects were calculated in two distinct steps. The external radiative process, which is the finite probability that the incoming or scattered electron will radiate a hard photon in the presence of a nucleon in the target other than the one associated with the event, is taken into account during the Monte Carlo acceptance calculation. The internal radiative corrections include the Bremsstrahlung process for the incoming or scattered electron in the presence of the nucleon associated with the event, as well as diagrams such as vacuum polarization, which are not accounted for during the acceptance calculation. These are included in the correction factor $F_{\rm rad}$ using the radiative correction code EXCLURAD and setting the controlling parameter $v_{\rm cut} = 0.047$ GeV^2 [35]. $F_{\rm rad}$ is calculated in each W and Φ bin as the ratio $\sigma_{\rm rad}/\sigma_{\rm norad}$ (variable δ in Eq. (75) from Ref. [35]), where $\sigma_{\rm norad}$ is the cross section calculated without any radiative effects (i.e., the

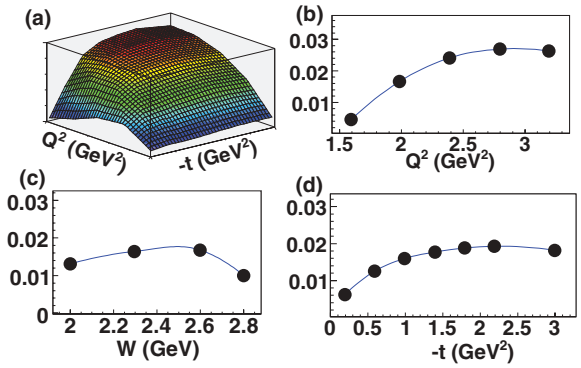

FIG. 8. (Color online) 2-D acceptance in Q^2 and t, as well as the 1-D acceptance in Q^2, W, and $-t$. Error bars are not shown; the lines are present to guide the eye. The axes in the 2-D plot in (a) have the same range as that of the axis of the two 1-D plots in (b) and (d).

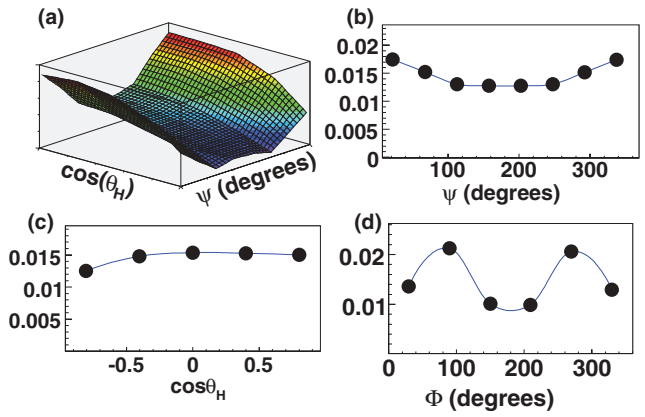

FIG. 9. (Color online) 2-D acceptance in $\cos\theta_H$ and ψ, as well as the 1-D acceptance in $\cos\theta_H$, Φ, and ψ. Error bars are not shown; the lines are present to guide the eye. The axes in the 2-D plot in (a) have the same range as that of the axis of the two 1-D plots in (b) and (c).

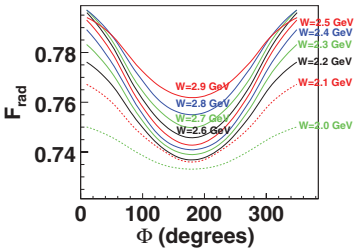

FIG. 10. (Color online) Radiative correction $F_{\rm rad}$ as a function of Φ for assorted values of W from 2.0 to 3.0 GeV. The correction for each W value was computed for $\langle Q^2\rangle = 2.47$ GeV^2 and $\langle \cos\theta_{c.m.}\rangle = 0.345$.

Born cross section) and $\sigma_{\rm rad}$ is the cross section calculated with radiative effects included. The correction factor for various W bins is shown as a function of Φ in Fig. 10. The correction was computed in bins of W and Φ for average values of Q^2 and $\cos\theta_{\rm c.m.}$ (directly related to $-t$) because the correction was found to change less than 2% over the range of Q^2 and $\cos\theta_{\rm c.m.}$ [36].

VII. CROSS SECTIONS

The reduced $\gamma^* p \to \phi p$ electroproduction cross section is given by

$$\sigma(Q^2, W) = \frac{1}{\Gamma(Q^2, W, E_e)} \frac{d\sigma}{dQ^2\, dW},$$
$$\Gamma(Q^2, W, E_e) = \frac{\alpha}{4\pi} \frac{W\left(W^2 - M_p^2\right)}{M_p^2 E_e^2 Q^2} \frac{1}{1-\epsilon}, \tag{6}$$

where $\Gamma(Q^2, W, E_e)$ is the virtual photon flux factor. We can extract the ϕ cross section from the data via

$$\frac{d\sigma}{dQ^2\, dW} = \frac{1}{\rm Br} \frac{n_W}{\mathcal{L}_{\rm int} \Delta Q^2 \Delta W}, \tag{7}$$

where Br is the branching fraction ratio of $\phi \to K^+K^- = 0.491 \pm 0.009$ [33], $\mathcal{L}_{\rm int} = 2.98 \times 10^{40}$ cm^{-2} is the live-time-corrected integrated luminosity, ΔQ^2 and ΔW are the corresponding bin widths modified appropriately when not completely filled due to kinematics, and n_W is the result of a fit to the M_{KK} distribution weighted by acceptance, CC efficiency correction, and radiative corrections. The binning in Q^2, $-t$, t', and W for the extraction of the cross section in those variables is shown in Table II. We emphasize here that we have performed a fit to Eq. (3) to determine the signal n_W and the estimated background under the peak for each entry in the table. The differential cross section in a variable X is given as

$$\frac{d\sigma}{dX} = \frac{\sigma(Q^2)}{\Delta X}, \tag{8}$$

where $\sigma(Q^2)$ is the total cross section in a bin in X. The cross sections presented in this paper have been corrected for the bin size and are quoted at the center of each bin.

TABLE III. W range for each Q^2 bin.

Q^2 range	W range
$1.4 \leqslant Q^2 \leqslant 1.8$	$2.10 \leqslant W \leqslant 2.90$
$1.8 \leqslant Q^2 \leqslant 2.2$	$2.10 \leqslant W \leqslant 2.90$
$2.2 \leqslant Q^2 \leqslant 2.6$	$2.10 \leqslant W \leqslant 2.90$
$2.6 \leqslant Q^2 \leqslant 3.0$	$2.10 \leqslant W \leqslant 2.70$
$3.0 \leqslant Q^2 \leqslant 3.8$	$2.10 \leqslant W \leqslant 2.70$

A. Total cross section $\sigma(Q^2)$

The cross section $\sigma(Q^2)$ as a function of Q^2 is obtained by integrating over W due to the limited statistics. Each event was weighted for acceptance, radiative effects, CC efficiency, and the virtual photon flux factor. The invariant mass distribution M_{KK} of weighted events in each Q^2 bin was then fitted to Eq. (3). The bins used in the analysis are given in Table III. The range in W was restricted at the low end where acceptance corrections change rapidly and are large, and at the high end to match the high end of the kinematically accessible range.

The cross section for each of the bins was calculated according to Eqs. (6) and (7). A small correction (∼1–2%) was then applied to adjust the bin-averaged cross section to the center of the bin [37]. The values for the cross section in each Q^2 bin are shown in Table IV. The total cross section was fit to the function

$$\frac{A}{\left(Q^2 + M_\phi^2\right)^n} \tag{9}$$

to determine the scaling behavior. For these data, we determined the parameter $n = 1.97 \pm 0.84$. The measured exponent spans the range expected for the dependence on Q^2 due to VDM ($n = 2$) to hard scattering ($n = 3$ for fixed momentum transfer t).

B. Differential cross section in t', $d\sigma/dt'$

The differential cross section in t' was extracted in seven bins in t' by fitting Eq. (3) to the K^+K^- mass distribution to determine the ϕ signal and background in that particular bin. The average χ^2 per degree of freedom for these fits was 1.2. The signal-to-background ratio varied from bin to bin, ranging from 0.33 to 0.86. The lowest signal-to-background ratio occurred in the midrange of t'. The resulting values for the cross section in each t' bin are shown in Table V.

TABLE IV. Total cross section $\sigma(Q^2)$ and kinematics of each data point, along with the center of each Q^2 bin. $\langle\epsilon\rangle$ is the average virtual photon polarization in each bin.

Q^2 (GeV^2)	$\langle\epsilon\rangle$	σ (nb)
1.6	0.488	9.9 ± 3.2
2.0	0.479	10.4 ± 2.5
2.4	0.471	6.7 ± 1.9
2.8	0.464	5.9 ± 2.4
3.4	0.452	3.6 ± 1.8

TABLE V. Differential cross section $d\sigma/dt'$ and kinematics of each data point. t' is the center of the bin, and corresponds to an average value of $\epsilon = 0.47$.

t' (GeV^2)	$d\sigma/dt'$ (nb/GeV^2)
0.1	9.4 ± 2.9
0.3	4.4 ± 1.9
0.5	3.1 ± 1.2
0.7	2.7 ± 1.2
0.9	4.0 ± 1.3
1.5	1.6 ± 0.4
2.8	0.5 ± 0.2

In cases of limited statistics, $d\sigma/dt'$ is often used instead of $d\sigma/dt$ in order to eliminate kinematic corrections due to $-t_0$, which varies with Q^2 and W. This procedure is most useful when the cross section factorizes into terms that depend only on t and terms that depend on Q^2 and W, aside from the threshold dependence, as in the VDM model. Indeed, our measured differential cross sections in t' show very similar trends as previous data, namely, they are consistent with diffractive production ($e^{-b_\phi|t'|}$) [22]. Figure 11 shows an exponential fit to the measured differential cross section, which yields a $b_\phi = 0.98 \pm 0.17$ GeV^{-2}. At high energies, the slope can be directly interpreted in terms of the transverse size of the interacting configuration, as described later when presenting results. In that limit, the small value of the exponential slope implies the interaction takes place at very short distances inside the nucleon.

C. Differential cross section in t, $d\sigma/dt$

The differential cross section is easiest to compare with theory if it is computed in terms of the Mandelstam variable t. The cross section is given as

$$\frac{d\sigma}{dt} = \frac{\sigma(Q^2)}{\Delta t \times \mathrm{Corr}(t_0)}, \tag{10}$$

where Δt is the bin size and $\mathrm{Corr}(t_0)$ is a correction factor to account for the fact that the kinematic limit $t_0(Q^2, W)$ varies across the bin. The yield was extracted over the ranges of Q^2 and W given in Table III in six bins in $-t$. The kinematic threshold t_0 varies between -0.09 and -1.14 GeV^2 for extreme values of Q^2 and W. For the bin corresponding to $0 \leqslant -t \leqslant 0.4$ GeV^2, the threshold varies so much that corrections could not be modeled reliably, so that bin was dropped. The first bin reported contains a significant correction, but it was included with an increased systematic error. Subsequent bins had small or no corrections. The values for the cross section in each $-t$ bin are given in Table VI.

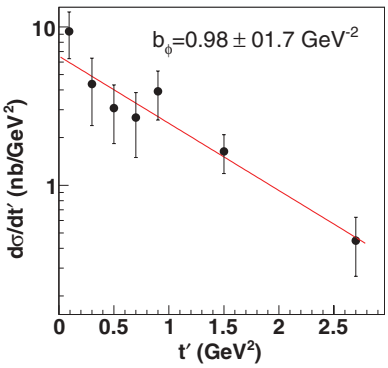

FIG. 11. (Color online) Plot of $d\sigma/dt'$ along with an exponential fit.

TABLE VI. Differential cross section $d\sigma/dt$ and kinematics of each data point. $-t$ is the center of each bin at an average value of $\epsilon = 0.47$.

$-t$ (GeV^2)	$d\sigma/dt$ (nb/ GeV^2)
0.6	10.7 ± 3.1
1.0	0.8 ± 1.0
1.4	3.4 ± 1.0
1.8	1.0 ± 0.5
2.2	1.4 ± 0.5
3.0	0.5 ± 0.2

D. Differential cross section $d\sigma/d\Phi$ and test of SCHC

The cross section dependence on the angle Φ between the electron and hadron scattering planes takes the form

$$\frac{d\sigma}{d\Phi} = \frac{1}{2\pi}(\sigma + \epsilon\sigma_{TT}\cos 2\Phi + \sqrt{2\epsilon(1+\epsilon)}\sigma_{LT}\cos\Phi), \tag{11}$$

where σ_{LT} and σ_{TT} are the interference terms between the longitudinal and transverse contributions to the cross section. If helicity is conserved in the s channel (SCHC), then both of these terms will vanish. The magnitude of these interference terms can therefore be used as a test for the validity of SCHC.

The differential cross sections in Φ were extracted in the same manner as the other differential cross sections [Eq. (8)] after integrating over Q^2, $-t$, and W. The cross section $d\sigma/d\Phi$ was extracted in six bins in Φ. The cross sections, along with a fit to Eq. (11), are shown in Fig. 12. The fit yields a value of $\sigma_{TT} = -1.1 \pm 3.1$ nb and $\sigma_{LT} = 2.2 \pm 1.1$ nb with a chi-squared per degree-of-freedom of $\chi^2/\mathrm{D.F.} = 1.3$. A fit of the

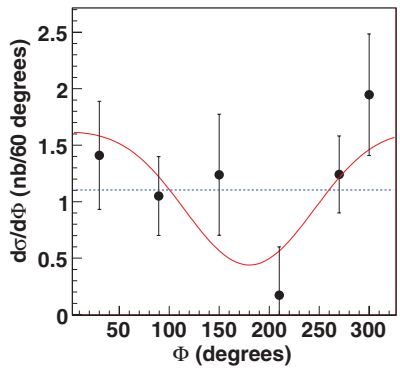

FIG. 12. (Color online) $d\sigma/d\Phi$ vs Φ. The curve shows a fit to Eq. (11) which is used to determine σ_{TT} and σ_{LT}. The dotted line is a fit to a constant function which is expected from SCHC.

$d\sigma/d\Phi$ distribution to a constant, constraining the interference terms to be zero, yields a χ^2/D.F. $= 1.6$. The small change in the goodness of fit between the two cases leads us to conclude that the precision of this experiment is insensitive to violations of SCHC for ϕ-meson production in our kinematic domain.

VIII. ANGULAR DECAY DISTRIBUTIONS

The angular decay distribution of the K^+ in the ϕ rest frame describes the polarization properties of the ϕ meson. The scattering amplitude for vector meson electroproduction $\gamma^* + N \to P + V$ can be expressed in terms of the helicity amplitudes $T_{\lambda_V \lambda_P \lambda_{\gamma^*} \lambda_N}$, where λ_i is the helicity of each particle ($i = V, P, \gamma, N$). The vector meson spin density matrix is derived from these helicity amplitudes by exploiting the von Neumann formula

$$\rho(V) = \tfrac{1}{2} T \rho(\gamma^*) T^\dagger, \tag{12}$$

where $\rho(\gamma^*)$ is the spin-density matrix of the virtual photon. The details of this derivation can be found in Ref. [28]. The density matrix element is denoted ρ^α_{ij}, where the index α can be related to the virtual photon polarization: $\alpha = 0{-}2$ for purely transverse photons, $\alpha = 4$ for purely longitudinal photons, while other values correspond to longitudinal-transverse interference terms. The indices ij correspond to the helicity state of the vector meson [38]. When the data do not allow for a σ_L/σ_T separation, the unseparated matrix elements r^α_{ij} can be parametrized as

$$r^{04}_{ij} = \frac{\rho^0_{ij} + \epsilon R \rho^4_{ij}}{1 + \epsilon R}, \tag{13}$$

$$r^\alpha_{ij} = \frac{\rho^\alpha_{ij}}{1 + \epsilon R}, \quad \alpha = 0{-}3, \tag{14}$$

$$r^\alpha_{ij} = \sqrt{R}\frac{\rho^\alpha_{ij}}{1 + \epsilon R}, \quad \alpha = 5{-}8. \tag{15}$$

Recall that R is the ratio of longitudinal to transverse cross section. The angular distribution of the K^+ is usually described in the helicity frame, defined in the rest frame of the ϕ meson with the z axis oriented along the ϕ meson in the $\gamma^* p$ center-of-mass. The full decay distribution, which we denote by $W_F(\cos\theta_H, \Phi, \phi_H)$, can be found in the literature [39] but will only be given here in simplified forms. In particular, further analysis of angular distributions is done under the assumption of SCHC, which leads to considerable simplifications with the introduction of $\psi = \phi_H - \Phi$ and the following constraints:

$$-\mathrm{Im} r^6_{10} = \mathrm{Re}\, r^5_{10} = \frac{\sqrt{R}\cos\delta}{\sqrt{8}(1 + \epsilon R)}, \tag{16}$$

$$r^1_{1-1} = -\mathrm{Im}\, r^2{}_{1-1} = \frac{1}{2(1 + \epsilon R)}, \tag{17}$$

$$r^{04}_{00} = \frac{\epsilon R}{1 + \epsilon R}. \tag{18}$$

All other r^α_{ij}'s are 0, and $\sqrt{R}e^{i\delta}$ is the ratio of the longitudinal to transverse amplitudes. The angular distribution becomes a function of two variables only and is given by

$$W(\cos\theta_H, \psi) = \frac{3}{8\pi}\frac{1}{1 + \epsilon R}\big[\sin^2\theta_H + 2\epsilon R \cos^2\theta_H - 2(1 + \epsilon R)\epsilon\big(r^1_{1-1}\big)\sin^2\theta_H \cos 2\psi + 4(1 + \epsilon R)\sqrt{\epsilon(1 + \epsilon)} \times \big(\mathrm{Re}\, r^5_{10}\big)\sin 2\theta_H \cos\psi\big]. \tag{19}$$

To extract the r^α_{ij} parameters from the measured angular distribution, we use two one-dimensional projections of the full angular distribution.

A. Polar angular distribution projection

To obtain the polar angular distribution, an integration of the full angular distribution W_F over ϕ_H yields

$$W(\cos\theta_H) = \tfrac{3}{4}\big[\big(1 - r^{04}_{00}\big) + \big(3r^{04}_{00} - 1\big)\cos^2\theta_H\big], \tag{20}$$

which is independent of SCHC. To obtain this projection from the data, the K^+K^- invariant mass distribution is plotted in five bins in $\cos\theta_H$ (0.40 units of $\cos\theta_H$ each). The same fit to a Gaussian plus a polynomial background was made to extract the weighted yields in each of these bins. The fit to $d\sigma/d\cos\theta_H$ in Fig. 13 yields a value $r^{04}_{00} = 0.33 \pm 0.12$ with χ^2/D.F. $= 1.7$. With the additional assumption of SCHC, this parameter can be used to determine the ratio of the longitudinal to transverse cross sections as

$$R = \frac{r^{04}_{00}}{\epsilon\big(1 - r^{04}_{00}\big)} = 1.05 \pm 0.38, \tag{21}$$

where we have used the average value of $\langle\epsilon\rangle = 0.47$.

B. Angular distribution projection in ψ

After an integration of W_F in $\cos\theta_H$, a substitution of $\phi_H = \psi + \Phi$, and an integration in Φ, the projected angular

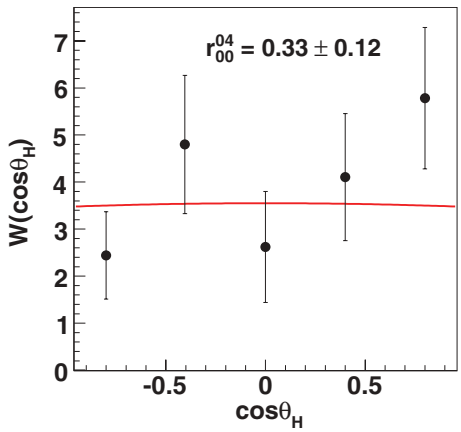

FIG. 13. (Color online) Unnormalized polar angular decay distribution of the K^+ integrated over all Q^2 values plus a fit to Eq. (20). Also shown is the extracted r^{04}_{00} parameter.

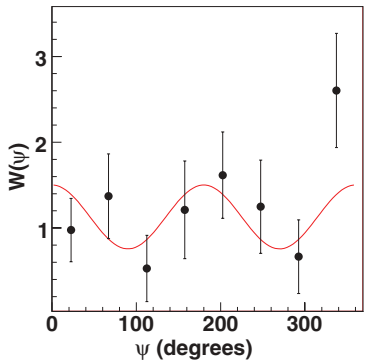

FIG. 14. (Color online) Unnormalized azimuthal angular distribution extracted for all Q^2 values plus a fit to Eq. (22). The value of r^1_{1-1} can also be used to determine R.

distribution in ψ is given as

$$W(\psi) = \frac{1}{2\pi}\left[1 + 2\epsilon\left(r^1_{1-1}\right)\cos 2\psi\right], \tag{22}$$

which assumes SCHC. The factor of $1/2\pi$ is a normalization factor. A fit of $d\sigma/d\psi$ to Eq. (22) is shown in Fig. 14. The fit yields a value $r^1_{1-1} = 0.38 \pm 0.23$ with a χ^2/D.F. $= 1.3$. The ratio of longitudinal to transverse cross sections can also be computed from r^1_{1-1} [Eq. (17)] and gives $R = 0.72 \pm 0.3$, in agreement with the value obtained previously.

IX. SYSTEMATIC UNCERTAINTIES

The relatively low number of measured ϕ events causes statistical errors to dominate. The sources of systematic errors in this experiment are summarized in Table VII. The major sources of systematic errors are due to acceptance corrections and estimation of backgrounds. Studies of backgrounds and their uncertainties were also limited by the finite sample size. The total systematic error of 18.6% was added in quadrature with the statistical errors in all quoted cross sections.

The acceptance correction contributes to the systematic error in two distinct ways. The uncertainty of 6% introduced by eliminating events with very large weights (i.e., very low acceptance) was estimated by changing the maximum weight allowed and recomputing the extracted cross section. The uncertainties introduced by the use of our acceptance table (12%) were estimated by combining bins and comparing the extracted result to the average of the constituent bins.

TABLE VII. Systematic errors.

Source	$\Delta\sigma$ (%)
Acceptance correction	13.4
Background functional form	9.1
Misidentified pion background	7.0
$epK^+(X)$ cut	5.0
Bin centering correction	1.0
Radiative correction	3.0
CC efficiency correction	1.0
Total	18.6

To estimate the systematic uncertainty due to the unknown distribution of backgrounds, the functional form of the background [see Eq. (3)] was modified by adding a term proportional to $(M^3_{KK} - M^3_{\rm th})$ and refitting the $-t$ and Q^2 distributions. The new fits were less constrained, but the average change in cross section was 9%. We found that the extraction of the slope parameter b_ϕ was fairly robust to these changes. In addition, the fitted invariant mass distributions included some background due to misidentified pions. The estimated uncertainty due to this contamination under the peak was estimated to be 7%.

The systematic uncertainty in the placement of the cut to select the K^- from the epK^+ missing mass (5%) was investigated by varying the cut and observing the effect on the cross sections. The systematic error associated with the bin centering correction is almost negligible ($\sim$1%). The contribution to the systematic error from the radiative correction was estimated to be $\sim$3% and is described in more detail in Ref. [35]. The fluctuation in the number of photoelectrons in the Cherenkov counter over the course of the run can cause a systematic error in the CC efficiency correction. This leads to a systematic of $\leq$1%. Finally, the procedure to estimate the correction due to the t_0 kinematic cutoff in the first t bin introduces a 25% systematic error in that bin.

X. DISCUSSION

The measurements of $\sigma(Q^2)$ from the present analysis are shown along with other data on ϕ electroproduction [20–23, 26] in Fig. 15. The one overlap point at $Q^2 = 1.5$ GeV^2 is in good agreement with the previous CLAS measurement [22]. The data sets span the range from threshold at $W = 2$ GeV up to HERA energies.

The data sets have a similar trend as a function of Q^2 and increase monotonically as a function of W. The three curves using the JML model at $W = 2.1$, 2.45, and 2.9 GeV are also plotted for Q^2 greater than 1.5 GeV^2. The calculation for

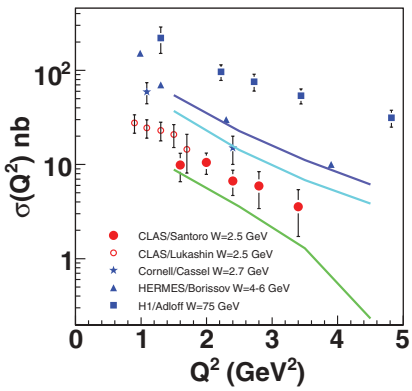

FIG. 15. (Color online) Total cross sections as a function of Q^2 for our data (red full circles), previous JLab data (open circles) [22], Cornell data (stars) for W between 2 and 3.7 GeV [21], HERMES data (triangles) for W between 4 and 6 GeV [23], and HERA data (squares) at high W [26]. The curves show the predictions of the JML model at $W = 2.9$, 2.45, and 2.1 GeV (top to bottom).

$W = 2.45$ GeV, which is close to the average of our data, seems to overestimate our data by about a factor of 2, although it does reproduce the existing Cornell data from Ref. [21]. The Cornell data set has a much wider acceptance range in W between 2.0 and 3.7 GeV, so in fact it could be representative of the cross section at higher W. The new data from CLAS, together with the existing world data, in particular the data from HERA, indicate that the qualitative behavior as a function of Q^2 does not change between threshold and a W of about 100 GeV.

Of interest is the applicability of factorization and the formalism of GPDs to meson production in general and ϕ production in particular. QCD factorization makes certain asymptotic predictions about the cross section, namely, that the longitudinal part of the cross section, σ_L, becomes dominant as Q^2 increases, and that the differential cross section will scale as $1/(Q^2)^3$ at fixed t and x_B. For a slow variation of the cross section over the range of x_B of the data (0.2–0.5), this prediction can be compared with the Q^2 dependence integrated over W and t, although quantitative estimates are modified by power corrections as well as kinematics near threshold. On the other hand, the VDM model predicts the cross section to scale as $1/(Q^2 + M_\phi^2)^n$ with $n = 2$. The Q^2 range of our data is limited, but in combination with previous CLAS data at lower Q^2 [22] (see Fig. 16), we can determine the scaling exponent of $1/(Q^2 + M_\phi^2)^n$ to be $n = 2.49 \pm 0.33$.

Present theoretical calculations of the ϕ production cross section based on GPD models suffer from considerable quantitative uncertainties when applied to fixed-target energies. At HERA energies, the approach taken in Ref. [40], which relies on the equivalence of leading-order QCD factorization with the dipole picture of high-energy scattering, gives a good description of the absolute cross section, as well as of subtle features such as the change of the W and t dependence with Q^2. Essential for the success of this approach is the fact that the effective scale of the gluon GPD, $Q^2_{\rm eff}$, is considerably smaller than the external photon virtuality, Q^2, as has been confirmed by detailed quantitative studies [41]. The same is expected in vector meson production at fixed-target energies; however, implementing it in a consistent manner in these kinematics has so far proven to be difficult. Leading-twist, leading-order QCD calculations of the ϕ production cross section at JLab and HERMES energies done with the assumption that $Q^2_{\rm eff} = Q^2$ [7] overestimate the measured cross section by a factor of 5–10 and predict too steep an energy dependence. A satisfactory solution to this problem likely requires a comprehensive approach that combines contributions from small-size ($\sim 1/Q$) and hadronic-size configurations in the virtual photon at moderate coherence lengths ($c\tau \lesssim 1$fm), and possibly higher order (next-to-leading order) QCD corrections. We note that a modified perturbative approach [8] that includes the intrinsic transverse momentum in the meson wave function has been fairly successful in reproducing the measured cross sections down to relatively low Q^2 and W.

The four-momentum transfer distribution probes the size of the interaction volume. At high energies, the exponential slope (see Fig. 11) is directly related to the transverse size $b_\phi \sim \frac{1}{3} R^2_{\rm int}$ in analogy to the classical scattering of light through an aperture of radius $R_{\rm int} \sim 0.38$ fm. At energies close to threshold, as in the present experiment, this interpretation requires some modification. When the coherence length becomes comparable to the size of the target, longitudinal shrinkage occurs, and this also causes a decrease of the exponential slope. The longitudinal size is related to the fluctuation time $\Delta\tau$ of the virtual meson, which can be estimated through uncertainty principle arguments, and is given by Eq. (1). The nature of the interaction becomes more point-like as Q^2 increases and the fluctuation time decreases. This transition should be observed as a decrease in the measured slope parameter. Since the differential cross section in t' was extracted for all Q^2, the value for b_ϕ corresponds to the average value of $c\Delta\tau = 0.46$ fm. The slope parameters for various experiments are shown in Fig. 17 for the world data on ϕ electroproduction. The measured slower falloff of the t distribution, corresponding to the small slope parameter, is consistent with the expectation that short interaction time probes small $s\bar{s}$ dipoles.

The differential cross section in $-t$ is compared with the JML model in Fig. 18. The data cover $1.4 \leqslant Q^2 \leqslant 3.8$ GeV^2, and the JML model predictions [42] are plotted for fixed values of Q^2 from 1.6 to 5 GeV^2. The data tend to have a shallower slope than the calculation, but there is general agreement. This agreement is highly nontrivial since the few parameters of the model have been fixed at the real photon point and kept frozen in the virtual photon sector. Our data confirm both the Q^2 and $-t$ dependence of the cross section that are built into the dynamics of the $s\bar{s}$ loop and the two-gluon loop.

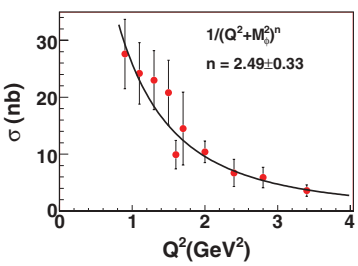

FIG. 16. (Color online) Fit to the cross section as a function of Q^2 distribution to determine scaling using data from the present experiment and CLAS data from Ref. [22].

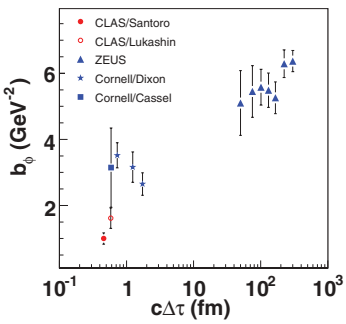

FIG. 17. (Color online) Exponential slope b_ϕ plotted as a function of the fluctuation parameters $c\Delta\tau$ for the world data. The data at high W measure an asymptotic slope corresponding to long fluctuation times. At low W and relatively large Q^2, the fluctuation times becomes small and constrain the size of the interaction volume.

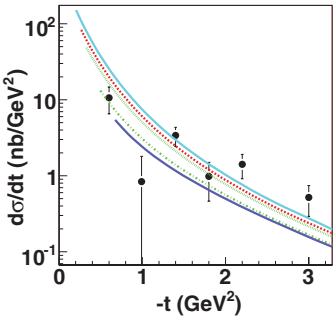

FIG. 18. (Color online) $d\sigma/dt$ vs $-t$ for the entire Q^2 range, and the JML predictions for $W = 2.5$ GeV at five values of $Q^2 =$ 1.6, 2.1, 2.6, 3.8, and 5 GeV^2, top to bottom.

The angular decay distributions provide information on the longitudinal part of the production cross section. We have extracted values of σ_{TT} and σ_{LT} from the cross section dependence on the angle Φ between the electron and hadron scattering planes. The value of the σ_{LT} is consistent with zero, and the assumption that SCHC is valid for ϕ production in this kinematic regime. However, small deviations are still possible as shown by more accurate measurements of these parameters at HERA energies [25].

The ratio $R = \sigma_L/\sigma_T$ has been determined from two projections of the angular decay distribution of the K^+ in the ϕ-meson rest frame and under the hypothesis of SCHC. The measurement of r^{04}_{00} gives $R = 1.05 \pm 0.38$, and the measurement of r^1_{1-1} gives a value of $R = 0.72 \pm 0.30$, the weighted average being $R = 0.85 \pm 0.24$. This measurement can be compared with the value of $R = 1.25$ predicted by the JML two-gluon exchange model. We note that these extractions, at least from r^{04}_{00}, are relatively insensitive to the assumption of SCHC as shown in Ref. [25].

The measurements of R from this analysis and other world data are plotted as a function of Q^2 in Fig. 19.[3] The data show that the ratio R is increasing as a function of Q^2, but σ_L is still not dominant at these kinematics. Using our measurement of R, we can compute the average longitudinal cross section for our data. The average cross section is given by $\sigma(Q^2 = 2.21\ \text{GeV}^2) = 6.9 \pm 1.7$ nb, which yields a longitudinal cross section $\sigma_L = 4.5 \pm 1.1$ nb.

[3]The W dependence of R has been studied at HERA [26], which covers a very large range in W.

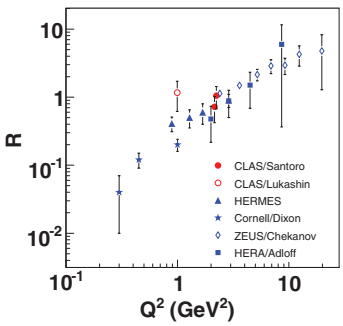

FIG. 19. (Color online) $R = \sigma_L/\sigma_T$ vs Q^2 for our data (solid circles), previous CLAS result (open circle), HERMES results (triangles), Cornell data (stars), ZEUS data (open diamonds), and HERA data (squares). The two determinations from the present analysis are separated for ease of viewing about the actual Q^2 value of 2.21 GeV^2.

XI. SUMMARY

ϕ-meson electroproduction was examined in the kinematic regime $1.4 \leqslant Q^2 \leqslant 3.8$ GeV^2, $0.0 \leqslant t' \leqslant 3.6$ GeV^2, and $2.0 \leqslant W \leqslant 3.0$ GeV. This data set doubles the range of Q^2 previously reported at JLab energies [22], accruing approximately four times the luminosity required for sensitivity to smaller cross sections. We have presented distributions as a function of the momentum transfer $-t$, the azimuthal angle Φ between the electron and hadron scattering planes, as well as angular decay distributions in the rest frame of the ϕ meson.

We have analyzed the angular distributions under the assumption of SCHC to extract the ratio of longitudinal to transverse cross sections of $R = 0.85 \pm 0.24$, which is consistent with the world trend. The longitudinal component is comparable to the transverse one, which suggests that we have not yet reached the asymptotic regime where QCD factorization can be applied without substantial corrections.

The cross sections have a weak dependence on $-t$, which indicates that at this Q^2, the photons couple to configurations of substantially smaller size than the target. Our data provide a very precise measurement of the exponential slope b_ϕ at small $c\Delta\tau \sim 0.5$ fm, which shows that we are probing very small distances, approaching about one-third the size of the proton itself. A natural explanation is that ϕ production is dominated by the scattering of small size $s\bar{s}$ virtual pairs off the target. This conclusion is supported by the good agreement between our data and the extension of the JML model from the real photon point (where it has been calibrated) to the virtual photon sector. It describes the interaction between this $s\bar{s}$ pair and the nucleon by the exchange of two dressed gluons. We conclude that these constituent degrees of freedom are appropriate for the description of ϕ-meson production at low W and $Q^2 \sim$ 2–3 GeV^2.

ACKNOWLEDGMENTS

We acknowledge the outstanding efforts of the staff of the Accelerator and the Physics Divisions at JLab that made this experiment possible. This work was supported in part by the U.S. Department of Energy, the National Science Foundation, the Italian Istituto Nazionale di Fisica Nucleare, the French Centre National de la Recherche Scientifique, the French Commissariat à l'Energie Atomique, and the Korean Science and Engineering Foundation. The Southeastern Universities Research Association (SURA) operated the Thomas Jefferson National Accelerator Facility for the United States Department of Energy under contract DE-AC05-84ER40150.

[1] J. Laget, Phys. Lett. **B489**, 313 (2000).
[2] J. Collins *et al.*, Phys. Rev. D **56**, 2982 (1997).
[3] B. Mecking *et al.*, Nucl. Instrum. Methods A **503**, 513 (2003).
[4] L. Morand *et al.*, Eur. Phys. J. A **24**, 445 (2005).
[5] M. Guidal and S. Morrow, in *Proceedings of the Exclusive Reactions at High Momentum Transfer*, 2007, Jefferson Lab [hep-ph 0711.3743].
[6] J. Santoro, Ph.D. thesis, Virginia Polytechnic Institute and State University, 2004.
[7] M. Diehl, W. Kugler, A. Schäfer, and C. Weiss, Phys. Rev. D **72**, 034034 (2005).
[8] S. V. Goloskokov and P. Kroll, Eur. Phys. J. C **50**, 829 (2007).
[9] J.-M. Laget and R. Mendez-Galain, Nucl. Phys. **A581**, 397 (1995).
[10] T. Bauer, R. Spital, and D. Yennie, Rev. Mod. Phys. **50**, 261 (1978).
[11] L. Frankfurt, M. Strikman, and C. Weiss, Annu. Rev. Nucl. Part. Sci. **55**, 403 (2005).
[12] J. M. Laget, Phys. Rev. D **70**, 054023 (2004).
[13] E. Anciant *et al.*, Phys. Rev. Lett. **85**, 4682 (2000).
[14] F. Cano and J. M. Laget, Phys. Rev. D **65**, 074022 (2002).
[15] F. Cano and J. Laget, Phys. Lett. **B551**, 317 (2003).
[16] L. Morand, Thèse de doctorat, Université Denis Diderot-Paris 7 (2003).
[17] C. Hadjidakis *et al.*, Phys. Lett. **B605**, 256 (2005).
[18] A. Airapetian, Eur. Phys. J. C **17**, 389 (2003).
[19] R. Dixon *et al.*, Phys. Rev. Lett. **39**, 516 (1977).
[20] R. Dixon *et al.*, Phys. Rev. D **19**, 3185 (1979).
[21] D. Cassel *et al.*, Phys. Rev. D **24**, 2787 (1981).
[22] K. Lukashin *et al.*, Phys. Rev. C **64**, 059901(E) (2001).
[23] A. Borissov, in *Proceedings of Meson 2000 Workshop*, Cracow, Poland, 2000 (unpublished).
[24] C. Adloff *et al.*, Z. Phys. C **75**, 607 (1997).
[25] C. Adloff *et al.*, Phys. Lett. **B483**, 360 (2000).
[26] S. Chekanov *et al.*, Nucl. Phys. **B718**, 3 (2005).
[27] J. Breitweg *et al.*, Eur. Phys. J. C **14**, 213 (2000).
[28] K. Schilling and G. Wolf, Nucl. Phys. **B61**, 381 (1973).
[29] M. Diehl, J. High Energy Phys. 09 (2007) 064.
[30] G. Adams *et al.*, Nucl. Instrum. Methods A **465**, 414 (2001).
[31] M. Amarian *et al.*, Nucl. Instrum. Methods A **460**, 239 (2001).
[32] E. Smith *et al.*, Nucl. Instrum. Methods A **432**, 265 (1999).
[33] W. Yao *et al.* (Particle Data Group), J. Phys. G **33**, 37 (2006).
[34] M. Holtrop *et al.*, GEANT simulation for CLAS, http://www.physics.unh.edu/maurik/gsim_info.shtml.
[35] A. Afanasev, I. Akushevich, V. Burkert, and K. Joo, Phys. Rev. D **66**, 074004 (2002).
[36] E. Smith and J. Santoro, CLAS-NOTE 2006-019, Jefferson Lab Hall B, 2006 (unpublished).
[37] E. Smith, CLAS-NOTE 2006-007, Jefferson Lab Hall B, 2006 (unpublished).
[38] S. Donnachie, G. Dosch, P. Landsoff, and O. Nachtmann, *Pomeron Physics and QCD*, Cambridge Monographs on Particle Physics, Nuclear Physics and Cosmology (Cambridge University, Cambridge, England, 2002).
[39] K. Schilling, P. Seyboth, and G. Wolf, Nucl. Phys. **B15**, 397 (1970).
[40] S. J. Brodsky, L. Frankfurt, J. F. Gunion, A. H. Mueller, and M. Strikman, Phys. Rev. D **50**, 3134 (1994).
[41] L. Frankfurt, W. Koepf, and M. Strikman, Phys. Rev. D **54**, 3194 (1996).
[42] J. Laget (private communication).